A 1 year mesoscale simulation of the northeast Atlantic: Mixed layer heat and mass budgets during the POMME experiment

H. Giordani,[1] G. Caniaux,[1] L. Prieur,[2] A. Paci,[1] and S. Giraud[3]

Received 15 October 2004; revised 13 April 2005; accepted 6 June 2005; published 26 July 2005.

[1] A simplified oceanic model is used to perform a realistic yearlong simulation to study fine-scale mixed layer processes in an area of the northeast Atlantic (21°–15°W, 38°–45°N) during the Programme Océan Multidisciplinaire Méso Echelle (POMME) experiment (September 2000–October 2001). This simplified three-dimensional oceanic model is obtained by degenerating the primitive equations system by prescribing continuously analysis-derived geostrophic currents $\mathbf{U}_g$ (called "guide") into the momentum equation by the substitution of the horizontal pressure gradient. The realism of the simulated mesoscale structures was validated by a comparison with in situ mesoscale and submesoscale data and results from the geostrophic adjustment to the guide. With this adjustment being applied at all scales, this model was able to simulate energetic small horizontal scales taking place around stirring eddies and frontal regions. Moreover, filamentary mixed layer depth structures were simulated and correlated to intense vertical velocities confined in the mixed layer. The circulation structure during POMME consisted of three quasi-permanent mesoscale eddies and a front. The mixed layer heat and mass budgets were thus strongly driven by the horizontal advection and the vertical transport associated with this mesoscale circulation. Although no effective detrainment or entrainment occurred at the domain scale, three regions were found to be the site of intense detrainment (around anticyclonic and cyclonic mesoscale eddies and along an axis of strong currents), in which the lateral induction and the vertical velocity at the mixed layer base are the major components driving the detrainment, respectively.

Citation: Giordani, H., G. Caniaux, L. Prieur, A. Paci, and S. Giraud (2005), A 1 year mesoscale simulation of the northeast Atlantic: Mixed layer heat and mass budgets during the POMME experiment, *J. Geophys. Res.*, *110*, C07S08, doi:10.1029/2004JC002765.

1. Introduction

[2] In order to capture the realistic evolution of mesoscale structures during yearlong simulations, regional models need to be coupled to an assimilation data system [*Lozano et al.*, 1996]. The majority of models use sequential assimilation systems which are efficient in reducing drifts and unrealistic circulations but induce mass circulation imbalances at each reinitialization procedure [*Robinson*, 1996]. Such imbalances produce shocks and the radiation of spurious gravity waves that is unappropriate for estimating time-integrated mixed layer budgets [*Gavart*, 1996]. Without the assimilation of satellite data, *Paci et al.* [2005] show that 3 months is a maximum duration for returning some degree of realism in an open lateral boundaries primitive equation (PE) model. Tests of long integrations in assimilation mode performed with a PE model have also shown a time degradation of the simulations induced by the lateral boundaries [*Gavart*, 1996]. In climate simulations, model drift is limited by using an interactive surface net heat flux correction toward a climatology [*Barnier et al.*, 1995]. This damping is a physical feature of the coupled ocean-atmosphere system and varies with the spatial scale of the sea surface temperature (SST) anomaly [*Drijfhout and Walsteijn*, 1998]. These results illustrate well the difficulty of performing realistic yearlong simulations with a regional high-resolution PE model. This paper aims to perform realistic yearlong simulations of the mixed layer at the mesoscale and submesoscale in order to conduct detailed studies on physical and biological processes. In order to reach this objective, *Giordani et al.* [2005] developed a simplified three-dimensional oceanic model by degenerating the primitive equation system by prescribing continuous analysis-derived geostrophic currents into the momentum equation by the substitution of the horizontal pressure gradient. This model assimilates geostrophic current maps according to a data direct insertion method described by *Robinson et al.* [1998] in order to prevent that the model

[1] Meteo-France/Centre National de Recherches Météorologiques/Groupe d'Etudes de l'Atmosphère Météorologique, Toulouse, France.
[2] Laboratoire d'Océanographie de Villefranche, Villefranche-sur-mer, France.
[3] Service Hydrologique et Océanographique de la Marine/Centre Militaire d'Océanographie/Recherche, Observatoire Midi-Pyrénées, Toulouse, France.

0148-0227/05/2004JC002765

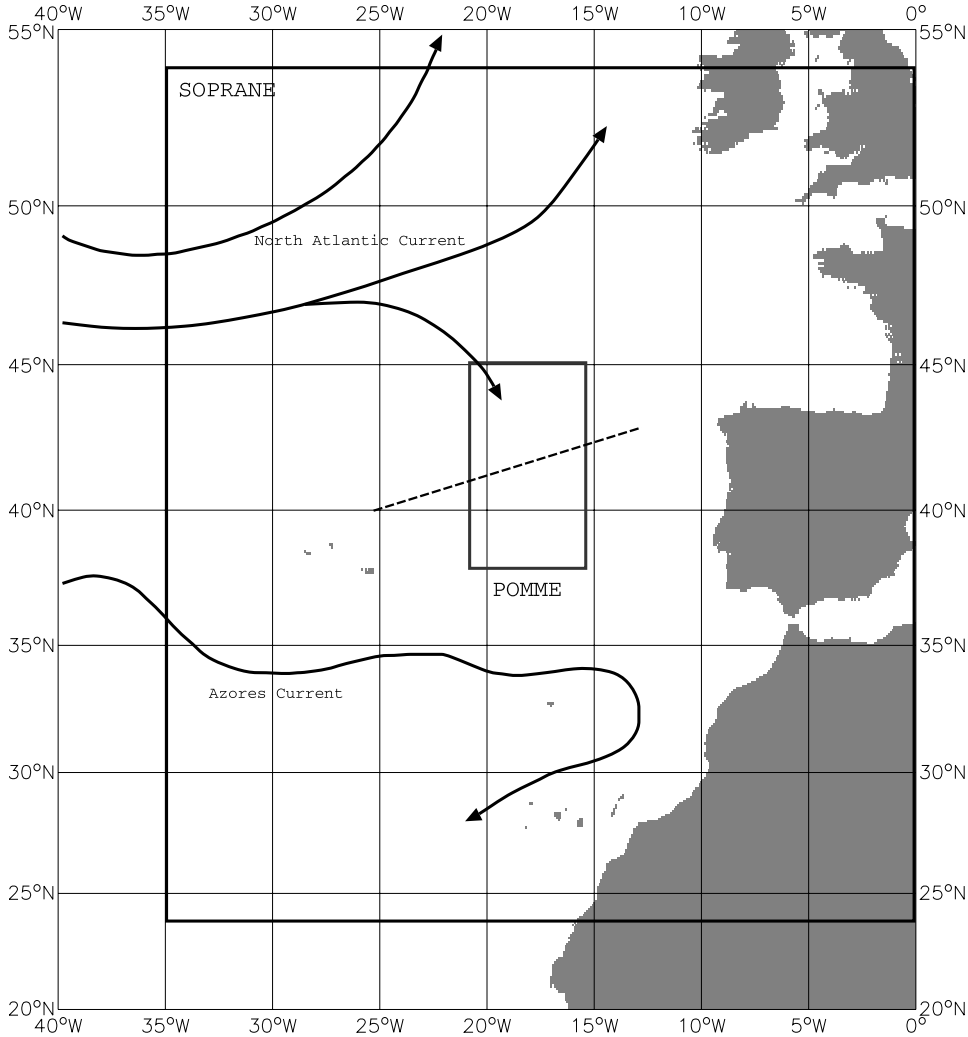

Figure 1. Positioning of the Programme Océan Multidisciplinaire Méso Echelle (POMME) experiment. The small rectangle represents the experimental and simulation domain. The large rectangle represents the simulation domain of the quasi-geostrophic model Système Océanique de Prévision Régionale en Atlantique Nord-Est (SOPRANE). The dashed line crossing the POMME domain symbolizes the climatological place of the mixed layer depth (MLD) front where the mode water subduction occurs.

develops a too chaotic/unrealistic flow. Simplification is provided by the time sequence of geostrophic currents, called "guide." This model was tested during a 50-day-long simulation during the period of the Programme Océan Multidisciplinaire Méso Echelle (POMME) [*Mémery et al.*, 2005] and its potential and preliminary results are presented by *Giordani et al.* [2005].

[3] The POMME experiment took place in the northeast Atlantic Ocean half way between the Azores and the Iberian Peninsula. The POMME domain, shown Figure 1, extends in longitude over 500 km between 15.33°W and 21.33°W and in latitude over 750 km between 38°N and 45°N. The experiment took place between September 2000 and September 2001. During this period, a multiparameter data set was collected at mesoscale spatial and temporal resolutions in order to understand the effects of mesoscale structures (diameters around 50–200 km) on 11°–13°C mode water subduction [*Paillet and Arhan*, 1996], the mixed layer heat budget and the spring bloom. Four oceanographic cruises were carried out during which the R/Vs *D'Entrecasteaux* and *Atalante* were used to perform hydrographic surveys covering the POMME domain at 50 km resolution. Conductivity-temperature-depth (CTD) measurements and bathythermograph (XBT) measurements between each CTD station were collected during each of the intensive hydrographic surveys POMME 0 (P0, September 2000), POMME 1 (P1, February 2001), POMME 2 (P2, April 2001), and POMME 3 (P3, September 2001), allowing for a description of the mesoscale features at a resolution of nearly twice the internal Rossby radius of deformation ($Ro \simeq 30$ km).

[4] This paper focuses on the validation and analysis of the main simulated components which constitute a realistic background for estimating the subduction at the mesoscale and submesoscale. Indeed, since no surface flux/mass relaxation and no mass field assimilation are used to drive this simplified model, we need to primarily validate the simulated mixed layer circulation and thermohaline struc-

tures at the mesoscale and submesoscale. After an accurate validation of the model, an evaluation of the integrated effects of the mesoscale and submesoscale structures on the mixed layer heat and detrainment/entrainment (hereafter called mass) budgets during POMME is proposed.

2. Experiment Design

[5] This section presents the model implementation in the POMME domain and the analyses and surface forcing used to initialize and force the model respectively.

2.1. Numerical Model and Implementation

[6] This model is based on a simplification of the primitive equation set which is carried out by replacing the horizontal pressure force in the momentum equation with the time sequence of geostrophic currents ($\mathbf{U}_g$). This simplification is possible due to the link between $\mathbf{U}_g$ and $\nabla_h P$ ($\mathbf{U}_g = (1/\rho f)\mathbf{k} \times \nabla_h P$). The complete simplified PE system detailed by *Giordani et al.* [2005] is written as follows:

$$\begin{cases} \dfrac{\partial \mathbf{U}_h}{\partial t} = -f\mathbf{k} \times \left(\mathbf{U}_h - \mathbf{U}_g\right) + \dfrac{\partial}{\partial z}\left(K\dfrac{\partial \mathbf{U}_h}{\partial z}\right) - (\mathbf{U}\cdot\nabla)\cdot\mathbf{U}_h \\ \dfrac{\partial T}{\partial t} = \dfrac{F_{\mathrm{sol}}}{\rho C_p}\dfrac{\partial I(z)}{\partial z} + \dfrac{\partial}{\partial z}\left(K\dfrac{\partial T}{\partial z}\right) - (\mathbf{U}\cdot\nabla T) \\ \dfrac{\partial S}{\partial t} = \dfrac{\partial}{\partial z}\left(K\dfrac{\partial S}{\partial z}\right) - (\mathbf{U}\cdot\nabla S) \\ \dfrac{\partial e_T}{\partial t} = \dfrac{\partial}{\partial z}\left(K\dfrac{\partial e_T}{\partial z}\right) + K\left(\dfrac{\partial \mathbf{U}_h}{\partial z}\right)^2 + \dfrac{g}{\rho}K\dfrac{\partial \rho}{\partial z} - C_\epsilon\dfrac{e_T^{3/2}}{l_\epsilon} \\ \dfrac{\partial w}{\partial z} = \dfrac{1}{(\zeta+f)}\left(\dfrac{\partial(\zeta+f)}{\partial t} + \mathbf{U}\cdot\nabla(\zeta+f)\right. \\ \qquad \left. + \dfrac{f}{\rho}\mathbf{U}_g\cdot\nabla_h\rho - \mathbf{k}\cdot\left(\dfrac{\partial \mathbf{U}_h}{\partial z}\times\nabla_h w\right) + \dfrac{\mathbf{k}}{\rho}\cdot\mathbf{Rot}\left(\dfrac{\partial \boldsymbol{\tau}}{\partial z}\right)\right) \\ \rho = \rho(T,S) \end{cases} \quad (1)$$

System (1) consists of the momentum equations, the temperature and salinity equations, the turbulent kinetic energy and vorticity equations and the full sea water state equation.

[7] $T(z)$, $S(z)$, $\mathbf{U}_h$, $\mathbf{U} = (\mathbf{U}_h, w)$ and ζ are the temperature, salinity, horizontal current, the total current and the vertical vorticity; w is the vertical velocity and f is the Coriolis parameter; ρ and C_p are the density and specific heat of sea water; $I(z)$ is the fraction of the net solar surface irradiance F_{sol} that penetrates to depth z; τ is the turbulent momentum flux; C_ϵ and l_ϵ are the coefficient of dissipation and the dissipative length scale; and $\mathbf{k}$ the vertical unit vector. The vertical mixing coefficient K is based on the calculation of two turbulent length scales representing upward and downward conversions of turbulent kinetic energy (e_T) into potential energy [*Bougeault and Lacarrère*, 1989]. This justifies the prognostic equation for the variable e_T. Finally, the vertical velocity is diagnosed from the vorticity equation.

[8] This model has to be coupled with systems providing gridded geostrophic currents, i.e., ocean circulation models, analyzed/reanalyzed fields or climatologies. $\mathbf{U}_g$ is estimated at each model time step by a temporal linear interpolation between two gridded analyzed maps. Interpolated $\mathbf{U}_g$ are directly inserted into the momentum and vorticity equations by a gradual and smooth assimilation procedure corresponding to a continuously data-driven simulation [*Lozano et al.*, 1996]. This operation degenerates the PE system through the removal of the pressure term. Consequently, this simplified system does not generate gravity waves and the simulated current $\mathbf{U}_h$ adjusts to $\mathbf{U}_g$ at the Coriolis frequency. Here the time sequence of $\mathbf{U}_g$ is used as a low-resolution and low-frequency interpolator which acts as a rigid guide or forcing term in the system. It is important to note that the T and S equations of system (1) are fully prognostic and unconstrained. The guide modifies the velocity that in turn affects T and S through the advection. The geostrophic guide does not constrain the T and S equations directly (as with relaxation methods) but gives rise to an ageostrophic circulation which tends to continuously balance the evolving mass fields with the prescribed geostrophic dynamics through the T and S equations. Therefore the simulated structures are dynamically consistent with this guide at all scales, particularly at smaller scales than the assimilated geostrophic current. Since the adjustment is not instantaneous, the simulated $\mathbf{U}_g$ (i.e., the spatial variability of ρ, $\nabla\rho$) is different from the assimilated $\mathbf{U}_g$. This difference is a source of thermal wind imbalance which appears explicitly in the baroclinic term of the vertical velocity equation (third term of the right hand side) of system (1). This term is not zero because $\mathbf{U}_g$ is not derived from the model mass field.

[9] The main advantage of this technique is to prevent strong drift during long simulations and shocks associated with sequential data assimilation [*Lermusiaux and Robinson*, 1999], both of which are essential for performing realistic mixed layer budgets over 1 year.

[10] Finally, the surface forcings are taken into account into the horizontal momentum, vertical velocity (curl of τ), temperature, salinity and turbulent kinetic energy equations through the vertical diffusive terms.

[11] This model is implemented in the POMME area extending over 500 km longitude from 21.33°W to 15.33°W and 750 km latitude from 38°N to 45°N (Figure 1) to simulate the ocean between P0 and P3. The horizontal regular grid spacing is 5 km, chosen in order to resolve the third Rossby baroclinic deformation radius. The z level vertical grid has 19 vertical levels covering a total depth of 1000 m with the first at 1 m below the surface and a grid mesh interval ranging from 10 m near the surface to 100 m near the model bottom layer, which is considered as being flat.

2.2. Open Lateral Boundaries

[12] One of the main difficulties in modelling a limited area of the ocean is the treatment of open lateral boundaries. One of the most pragmatic numerical methods consists of modifying the prognostic equations in a zone close to the boundary. As by *Caniaux and Planton* [1998], a Newtonian relaxation toward a large-scale field $\tilde{X}(i)$ can be applied to the prognostic variables X in a zone near the boundary with a damping coefficient $\alpha(i)$; i being the distance from the lateral boundary. Following *Leslie et al.* [1981], if X_p is the

prognostic part of the model, the final solution X_f is found using the following relation:

$$X_f = (1 - \alpha(i))X_p + \alpha(i)\tilde{X}(i),$$
$$\text{where } 0 \leq \alpha(i) \leq 1 \text{ for } 1 \leq i \leq N_{\text{relax}}.$$

[13] The number of relaxed rows N_{relax} from the lateral boundary was kept equal to one and $\alpha(1) = 1$ because the assimilation technique used does not generate spurious gravity waves in the simulation domain (see section 2.1 or *Giordani et al.* [2005]). Consequently, the large-scale information crosses the lateral boundaries into and out the domain through advection by the prescribed geostrophic current (radiative conditions). Note that this simplified model avoids the delicate computation of a propagative normal radiative velocity at the lateral boundaries usually used in regional PE models to minimize generation and reflection of gravity waves [*Carpenter*, 1982; *Xue and Thorpe*, 1991]. The specified values $\tilde{X}(i)$ on the boundaries of the simulation domain may be held constant in time or may be allowed to evolve.

2.3. Initialization Procedure

[14] Four hydrological surveys were used to produce high-resolution temperature and salinity analyses (hereafter called POMME analyses) from CTDs and XBTs. These data were first interpolated onto 65 vertical levels (of 5 m vertical resolution near the surface, 300 m at depth) and then objectively analyzed onto a 5 km horizontal grid for all vertical levels following the procedure used by *Caniaux and Planton* [1998] and *Dourado and Caniaux* [2001]. The first guess of the analyses was derived from the temperature and salinity *Levitus* [1982] climatology. At each grid point, the climatology was corrected using observations which lie within one influence time/space radius around the grid point, following the procedure of *de Mey and Ménard* [1989]. A space correlation radius of 50 km, consistent with the mesoscale structures, and a *e*-folding decay time of 10 days were chosen (following a compromise between salinity and temperature data) in order to time center each analysis to each mid survey date. Analyses were thus produced on 28 September 2000 (P0), 13 February 2001 (P1), 4 April (P2) and 4 September 2001 (P3), corresponding to the central dates of the four intensive observing periods. From these analyses, geostrophic currents were computed at each level through the thermal wind equation by using a level of no motion located near 1700 m [*Paci et al.*, 2005; *Giordani et al.*, 2005], which is close to that found by *Stramma* [1984] for the region considered in this paper.

[15] The initial mass and current fields of the model are produced by the temperature, salinity and geostrophic current analyses at P0, P1, P2 and P3. The annual simulation is thus composed of three simulations running between P0 and P1 (hereafter, S01); P1 and P2 (S12) and P2 and P3 (S23) each one lasting 139, 50 and 154 days respectively.

[16] Because of the significant evolution of the temperature and salinity during the POMME experiment, the large-scale information at the lateral boundaries were obtained by linear interpolation between two successive POMME analyses.

[17] Figure 2 displays the mesoscale cyclonic (CXX) and anticyclonic (AXX) eddies identified over the superimposed POMME SST and geostrophic currents analyzed maps (see section 2.3) at P0, P1, P2 and P3. Identification and the followup of the mesoscale eddy structures during POMME (P0, P1, P2, P3) has been carried out by *Le Cann et al.* [2005] and *Assenbaum and Reverdin* [2005]. The nomenclature adopted hereafter for the eddies is presented by *Mémery et al.* [2005].

[18] These structures, ranging typically between 50 and 200 km, slowly drift from the northeast toward the southwest during POMME as confirmed by *Le Cann et al.* [2005]. Some eddies rapidly leave the domain, like A3 (P0), A5 (P0) and C3 (P1), while others remained in the domain for a long time (6–7 months), like A1 (P0, P1, P2, P3), A2 (P0, P1, P2), A4 (P1, P2, P3), C2 (P0, P1, P2) and C4 (P0, P1, P2). In particular, eddies A1, C4 and A2 were quasi-permanent and structured the circulation during POMME.

[19] At P1, P2 and P3 (Figure 2), a surface thermal and circulation front is present between 40°N and 44°N. This front shows significant evolution induced by the displacement and deformation of the mesoscale eddies. Frontal current velocities reach 0.3 m s^{-1}.

2.4. Assimilated Currents: Système Océanique de Prévision Régionale en Atlantique Nord-Est Geostrophic Currents Fields

[20] Système Océanique de Prévision Régionale en Atlantique Nord-Est (SOPRANE) is an integrated regional operational forecasting system based on a quasi-geostrophic (QG) baroclinic model (10 layers, 1/10° horizontal resolution) which is derived from the *Blayo et al.* [1994] North Atlantic QG model. The model coverage extends from 35°W to the European and African coasts and from 24°N to 54°N (see Figure 1). It assimilates real-time fast delivery Sea Level Anomaly (SLA) data from TOPEX/Poseidon (T/P), JASON-1, ENVISAT and Geosat Follow-On altimeters. The so-called SOFA assimilation method [*de Mey and Benkiran*, 2000] is an optimal interpolation in a reduced space which assimilates the along-track data sequentially during a 1 week assimilation cycle. One of the authors (S. Giraud) carried out a reanalysis of the QG stream function for the period from 1993 to 2002 that consists in processing and assimilating improved along-track SLA computed by the CLS Space Oceanography Division using T/P, Jason-1 and ERS-1/2 data.

[21] During POMME, the reanalyzed stream functions were interpolated onto the grid of the model and then weekly SOPRANE analyses–geostrophic currents were derived over the simulation domain by finite differencing of the reanalyzed stream functions (hereafter called SOPRANE analyses).

[22] During simulations S01, S12, and S23, the geostrophic currents were specified from the POMME and SOPRANE analyses. At each time step of the model, geostrophic currents were linearly interpolated between two current analyses networks at every grid point and inserted into the momentum equation of system (1). Given that SOPRANE analyzed fields are available weekly, the linear interpolation gives a reasonable estimate of the geostrophic guide at each time step.

[23] The QG SOPRANE system produced the slow manifold of the circulation used as background in our

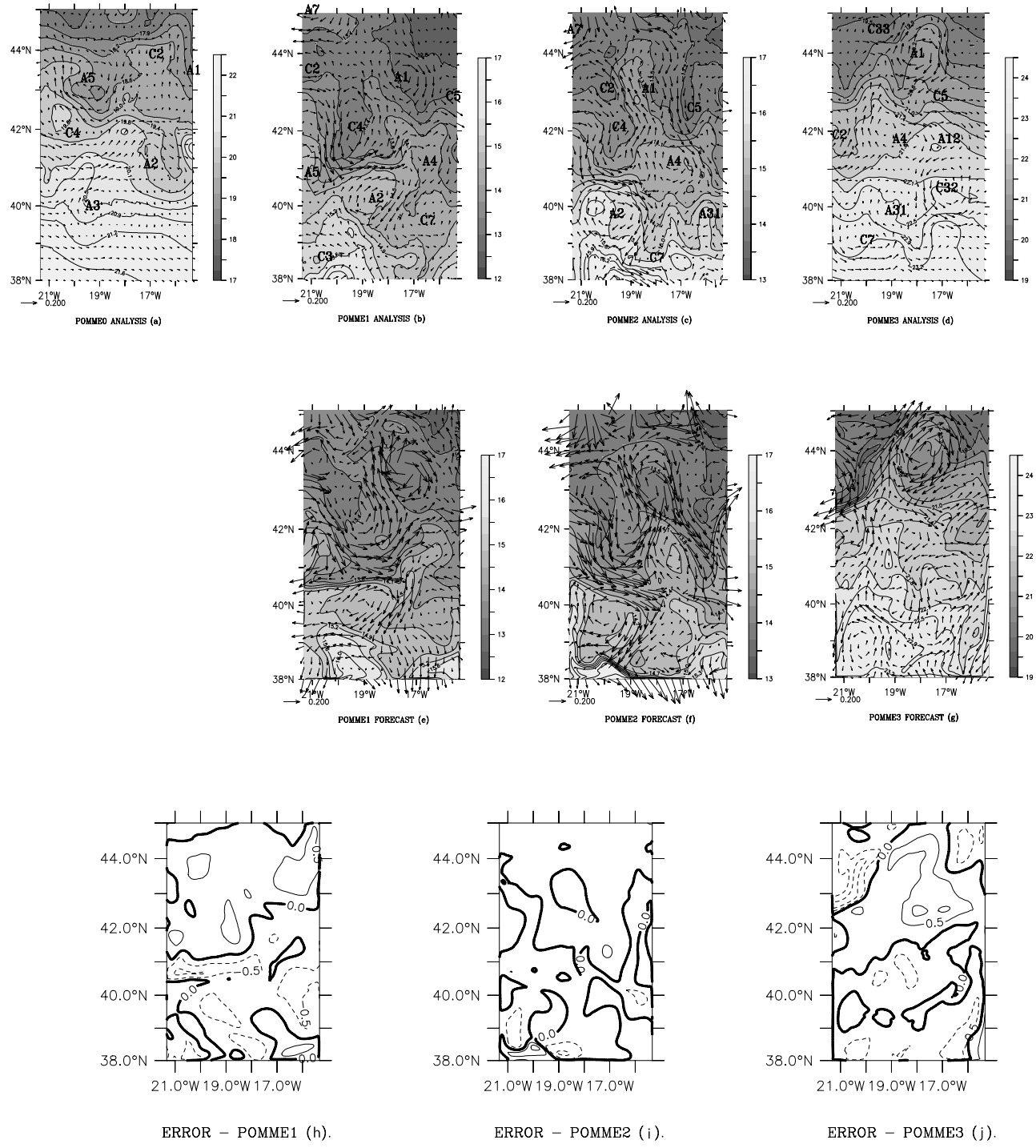

Figure 2. Analyzed sea surface temperature (SST) (C) and surface geostrophic current (m s^{-1}) at (a) P0, (b) P1, (c) P2, and (d) P3 and simulated SST and surface currents at (e) P1, (f) P2, and (g) P3. Anticyclonic and cyclonic eddies are positioned over the analyzed fields. SST error fields are obtained from the difference between the simulation and the analyses at (h) POMME 1, (i) POMME 2, and (j) POMME 3.

simplified model which simulates the rapid and small-scale physics (upper active mixed layer, ageostrophic circulations in fronts and eddies).

[24] As for the mass fields, geostrophic currents at the lateral boundaries were obtained by linear interpolation between two successive SOPRANE analyses.

2.5. Atmospheric Surface Forcing

[25] Different data sets were used for surface net heat fluxes. Hourly surface irradiances (solar and downward longwave radiation fluxes) were derived from the geostationary Meteosat satellite data set collected at the Centre de Météorologie Spatiale (Meteo-France, Lannion) following

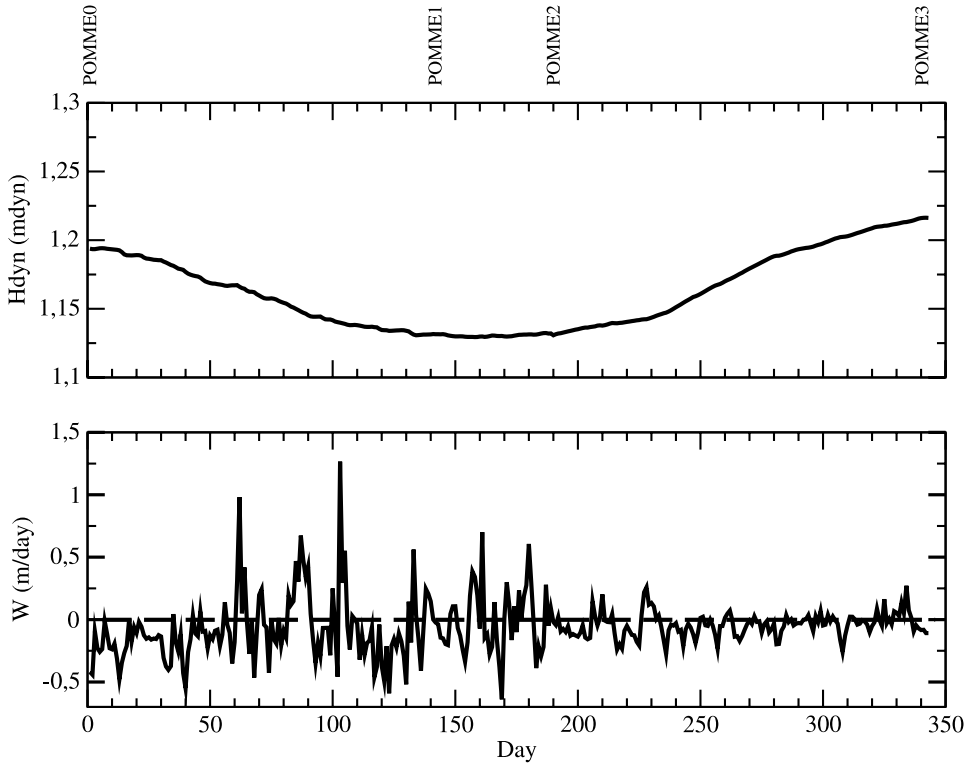

Figure 3. Annual evolution of the domain-averaged surface dynamic height (Hdyn) and vertical velocity at 50 m depth (*W*). POMME 0 (28 September), POMME 1 (13 February), POMME 2 (4 April), and POMME 3 (4 September).

the method developed by *Brisson et al.* [1994]. Solar and downward radiation fluxes available at a 4 km resolution were aggregated by averaging all available pixels 5 km around each model grid point.

[26] A large quantity of satellite-derived SST was available at a 2 km resolution. This data was processed and aggregated at the scale of the grid model (5 km) and merged with various in situ surface data fields in order to produce SST objective analyses every day during 1 year, (hereafter called satellite analyses [see *Caniaux et al.*, 2005a, 2005b]). These analyses were also used for validation of the model. The net longwave radiative surface flux was then obtained by subtracting the upward flux, computed with the satellite analyzed SST from the satellite downward radiation.

[27] Atmospheric parameters (temperature, specific humidity, surface wind, surface pressure and precipitation) of the ECMWF analyses available every 6 hours were interpolated onto the model grid and combined with analyzed satellite SSTs to compute the heat and momentum surface turbulent fluxes. These fluxes were calculated with a specific state-of-the-art bulk algorithm developed from the turbulence data collected during the POMME experiment [*Caniaux et al.*, 2005a]. The fluxes obtained were corrected using an optimization method based on a one dimensional oceanic model forced by lateral advection terms deduced from data, in order to balance the annual mixed layer heat content deduced from the POMME data [*Caniaux et al.*, 2005b].

[28] Time series of turbulent heat and momentum forcings display strong intermittencies which are associated with the passage of atmospheric depressions over the domain. The high resolution of the SST and atmospheric analyses restores a picture of the mesoscale structures of the turbulent surface fluxes [see *Caniaux et al.*, 2005b].

[29] The surface of the ocean model is forced with the daily estimates of penetrative solar radiation, radiative cooling, evaporation minus precipitation, sensible heat flux and wind stress.

3. Assimilation Impact

[30] The domain-averaged dynamic height evolution (Figure 3) shows how the assimilation of geostrophic currents impacts the model. The surface dynamic height (Hdyn) represents the integrated potential energy from the bottom (1000 m) up to the surface. It is important to note that the Hdyn evolution is continuous during the annual cycle during the weekly assimilation times and at the reinitialization procedure P1 and P2. Therefore this result shows that the assimilation technique used in this model does not generate shocks (and spurious induced structures by mass current imbalance) as in sequential assimilation [*Gavart*, 1996; *Gavart and de Mey*, 1997] and thus allows yearlong simulations. In this model, the surface dynamic height evolved in accordance with the assimilated geostrophic guide evolution. The guide tendency induces deformations and stretchings in the surface dynamic height field which are sources of vertical velocities (see section 5).

[31] Usually the sequential assimilation technique induces significant spin-up which affects preferentially the vertical velocity. The simulated domain-averaged vertical velocity (w) at 50 m shown in Figure 3 is confirmed by the surface

stress curl time series computed by *Caniaux et al.* [2005b]. Therefore the strong intermittencies simulated by the model are the result of the surface momentum forcing variability and are not linked to the assimilation procedure. Finally, the annual domain averaged w is negative (downward) and reaches -5.65×10^{-2} m d^{-1}, which is close to the downward Ekman motion computed by *Caniaux et al.* [2005b] (-5×10^{-2} m d^{-1}).

[32] Finally, Hdyn has an annual cycle (Figure 3) with high and low values in summer and winter respectively reflecting the annual cycle of the buoyancy flux. The value obtained at P3 is higher than the value at P0 because of stronger temperatures at P3 than at P0. This difference is representative of the interannual variability of the system [*Reverdin et al.*, 2005] and shows that the assimilation procedure used in this model does not induce energetic drifts.

4. Validation

[33] This section aims at testing the ability of the model to reproduce the mesoscale and submesoscale structures by the comparison the simulated mass and total current fields with independent data. Note that this model is constrained by the geostrophic guide but does not use relaxation on prognostic variables or surface fluxes. The data used is the in situ and satellite SST analyses, the thermosalinograph SST and SSS data and the processed currents data collected by the VMADCP.

4.1. Surface Fields Results

[34] This section presents the comparison of the simulated surface fields obtained at P1, P2 and P3 with the analyzed ones in order to validate the horizontal variability of the simulated thermal and dynamical structures near twice *Ro*.

[35] Figure 2 shows the SST and surface current field simulations for P1 (simulation S01), P2 (simulation S12) and P3 (simulation S23). S01, S12 and S23 simulate the ocean states during fall and winter time, late winter and spring, and spring and summer respectively.

[36] S01, S12 and S23 capture well the main mesoscale structures, which are the quasi-permanent eddies A1, C4 and A2 and the undulating thermal front with its associated zonal jet near 41°N. For example at P1, the thermal front and the associated zonal jet near 41°N were realistically (position and gradients) simulated by the model. This result is noteworthy because this front did not exist at the initial time and was created only by geostrophic adjustment during S01. The important point is the success of the model in simulating realistically the generation and the evolving positions of the main mesoscale dynamic structures during S01, S12 and S23 thanks to the mass adjustment around the geostrophic guide.

[37] Generally, the simulated currents are stronger than the analysis, particularly at P3 in the northwestern part of the domain. Two elements can explain this point: (1) the simulation displays the total current while the analysis displays the geostrophic current and (2) the simulated current is an instantaneous field that integrates strong Ekman currents that occurred at P3 (4 September 2001) while the analysis assimilated data is spread out over several days. During 3 days before P3, strong surface wind stress associated with shallow mixed layer depths ($\simeq$20 m) induced strong Ekman currents and negative net surface heat flux (not shown).

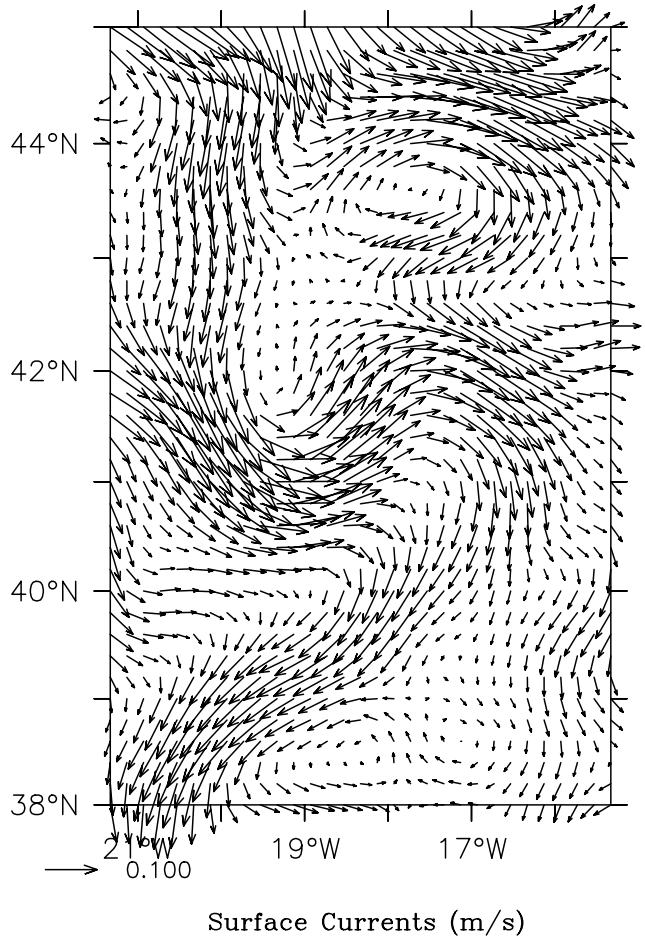

Figure 4. Annual averaged simulated surface currents.

[38] Biases of the simulated SSTs compared with the POMME analyses ranges between 0.5°C and −0.5°C (Figure 2). Stronger biases are observed at P3 because shallow mixed layer depths give to the SST a greater sensitivity to the mixed layer processes and long time (154 days) integrations are favorable to strong cumulative errors. These discrepancies are induced by the shifts in the simulated mesoscale structures compared to the analyzed ones but also by the nonsynopticity of the analyses. Indeed, sampling of in situ data over the domain spread over 20 days around the central time of each analysis induces space and time aliasing and nonsynopticity that affected the realism of the analyzed structures. Moreover, the optimal analysis technique uses a Gaussian temporal error covariance and isotropic structure functions to combine a first guess with data. This procedure is also a source of errors for the derived analyzed fields.

[39] The simulated surface currents (Figure 4) averaged over a year clearly show a southward circulation that is strongly affected by the eddies A1, C4 and A2. As mentioned in section 2.3, this results from the quasi-permanent positions of these three mesoscale structures during POMME. The yearlong average of the circulation produced by a simplified Kalman filter assimilating all the data collected during POMME [*Gaillard et al.*, 2005] confirms the simulated

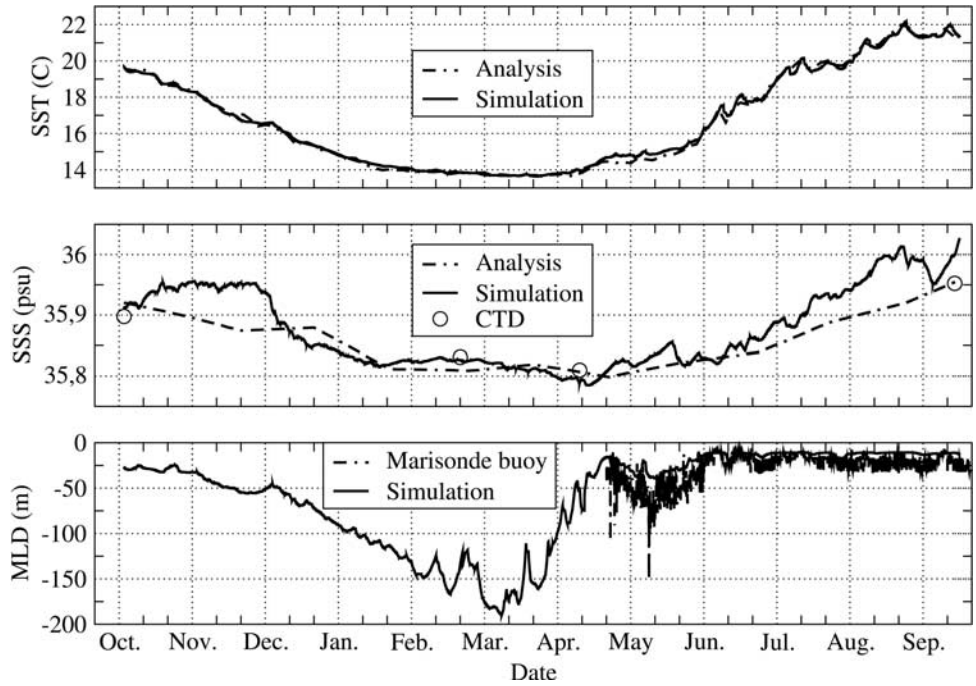

Figure 5. Annual evolution of the domain-averaged SST (°C), sea surface salinity (SSS) (psu), and MLD (m). Conductivity-temperature-depth (CTD) and Marisonde data were domain averaged in order to be compared with the model.

circulation shown Figure 4. This independent result validates the domain-scale circulation simulated by the model.

4.2. Time Series

[40] This section presents the comparison of the simulated surface fields with daily satellite analyses and surface measurements. This validation is more accurate than the previous one because the simulation is directly compared with original measurements. Such a comparison aims to check if the model is able to generate realistic submesoscale structures typically smaller than *Ro*.

4.2.1. Domain-Averaged Mixed Layer Parameters

[41] The simulated evolution of the spatially averaged SST, SSS and mixed layer depth (MLD) over POMME domain were evaluated by comparison with daily high-resolution SST analyses (see section 2.5) [*Caniaux et al.*, 2005b], monthly low-resolution (1° of longitude × 1° of latitude) SSS analyses (G. Reverdin et al., In situ surface salinity in the tropical and subtropical Atlantic ocean, part I: Large scale variability, submitted to *Climate Dynamics*, 2005), CTD and drifting buoys measurements (Figure 5).

[42] The simulation captures very well the SST decrease during the boreal fall and winter and the SST increase during the spring and summer. Both the amplitude of the annual cycle (8.2°C) and its higher frequency are well reconstructed by the model. Minima and maxima of simulated and observed SSTs reach 13.8°C around 10 March and 22°C around 22 August. The SSS evolution presents a seasonal cycle in agreement with the analyses. However, simulated SSS increases in October–November 2000 and in August 2001 have no equivalent in the analyses. Consequently, amplitudes of the analyzed and simulated annual cycles are of 0.15 psu and 0.2 psu, respectively. We have less confidence in the SSS analyses than on SST ones, due to their poor sampling and too coarse a resolution; consequently the comparison must be taken with care.

[43] The MLD is a relevant parameter for simulating realistic T, S and $\mathbf{U}_h$ in the upper layers and is a good diagnostic for the upper layer stratification. Figure 5 displays the simulated evolution of the domain-averaged MLD with superimposed buoy data. A simple criterion was adopted for the MLD of a change in density of 0.02 kg m^{-3} relative to the density at 12.5 m in order to avoid skin effects and diurnal cycles. The MLD varies from 11 m in summer to a maximum of 186 m in winter around 10 March. Although the mixed layer cooling and warming are symmetric in time, it is noteworthy to see that the associated mixed layer deepening/destratification in winter and the shallowing/restratification in spring and summer are considerably asymmetric. Indeed, the deepening spreads out over 6 months whereas the restratification lasts only 1.5 months. This well-known asymmetry [*Cushman-Roisin*, 1987] is confirmed by buoy data and CTD measurements and unidimensional simulations of the mixed layer during POMME [*Caniaux et al.*, 2005b]. This behavior is in agreement with the SST and MLD annual cycles observed in the eastern North Atlantic during the Subduction Experiment (June 1991–July 1993) and described by *Weller et al.* [2004] and *Spall et al.* [2000]. Finally, such asymmetry in the MLD annual cycle is suspected to play an important role in determining the effective period of subduction [*Cushman-Roisin*, 1987] and to capture the initial prebloom conditions and, later, the spring bloom evolution [*Fernández et al.*, 2005].

4.2.2. Thermosalinograph Data

[44] A fine spatiotemporal description of the SST and SSS in the POMME area was given by the thermosalinograph data collected along the ship route of the R/V

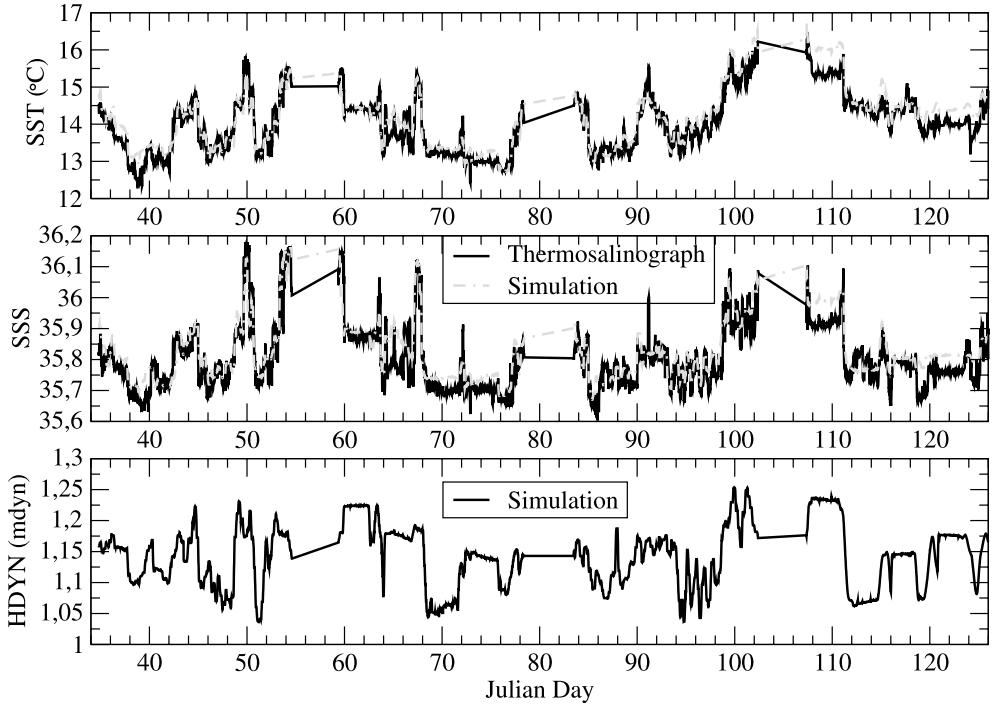

Figure 6. Comparison of the thermosalinograph measurements with the simulated SST (°C) and SSS (psu) along the ship trajectory. The simulated dynamic height (mdyn) along the ship trajectory is presented to show the correlation between Hdyn with the SSTs and SSSs.

L'Atalante between 13 February and 6 May. A complete description of the thermosalinograph data can be found by *Caniaux et al.* [2005a]. These SSTs and SSSs were sampled every 10 min and a validation of the simulation should have been performed on-line in the model in real-time with the observations. For yearlong simulations, the surface variables of the model were daily averaged and stored every day, for simplicity. Moreover, the surface fluxes used here do not include the diurnal cycle, thus justifying the daily averages. Consequently, all the observed data of a same day were compared to the corresponding daily-averaged simulated data. However, the time averaging procedure smoothes the simulated structures and induces uncertainties in their temporal locations at most equal to 24 hours which are sources of errors in the comparisons between the observed local data and the integrated simulated data. Thermosalinograph observations and simulated SST and SSS time series are displayed Figure 6. Bias, root mean squares (rms) and correlation coefficients between the observed and the simulated runs (7185 values) are 0.15°C, 0.34°C and 0.93 for the SST and 0.024 psu, 0.054 psu and 0.88 for the SSS, respectively. The high frequency of the observed data are not reproduced by the daily averaged simulated runs but the previous statistical parameters show that the model catches reasonably well the submesoscale structures ($5-10$ km $\leq Ro/3$) described by the thermosalinograph data. The correlation of the simulated SST and SSS with the simulated dynamic height reaches 0.65 and 0.75 respectively indicating that the geostrophic circulation drives strongly the surface thermohaline structures (Figure 6).

4.2.3. Local Validation of Mixed Layer Depth

[45] Since the heat and mass budgets are calculated over the mixed layer in this study, it is important to validate the MLDs. This validation is done through a local validation of the daily-averaged simulated MLD by comparison with the MLD deduced from CTD profiles collected along the ship track. The same criterion (described in section 4.2.1) was used for CTD and model data.

[46] This comparison, shown in Figure 7, is strongest because of the high temporal and spatial variability of the MLD fields, much larger than the ones of temperature, salinity and even horizontal currents fields shown in section 4.2.4. Moreover, the temporal frequency of the daily air-sea fluxes used may not be sufficient to reproduce the evolution of some in situ MLD. Indeed some diurnal variation in MLD of more than 100 m were observed between P1 and P2 (L. Merlivat, personal communication, 2005). Nonetheless, even if the comparison between CTD and simulated MLD shows that some MLD structures are missed by the simulation, the overall comparison is quite good, which is confirmed by a bias and a correlation coefficient between the two time series (347 values) of 10 m and 0.73 respectively. In particular, the variability is of the same magnitude in the CTD and simulated MLD, which is an important point indicating that the small MLD structures seen in Figure 10 are not likely to be numerical artefacts.

[47] There is no significant bias between observed and modeled fields, except for days 64–68. This period was largely composed of four CTD long stations, so that T and S evolution is more a temporal variation than a spatial variation and small errors in the localization of simulated thermohaline structures result in large discrepancies. Moreover these discrepancies are increased by the daily average of the simulated MLD.

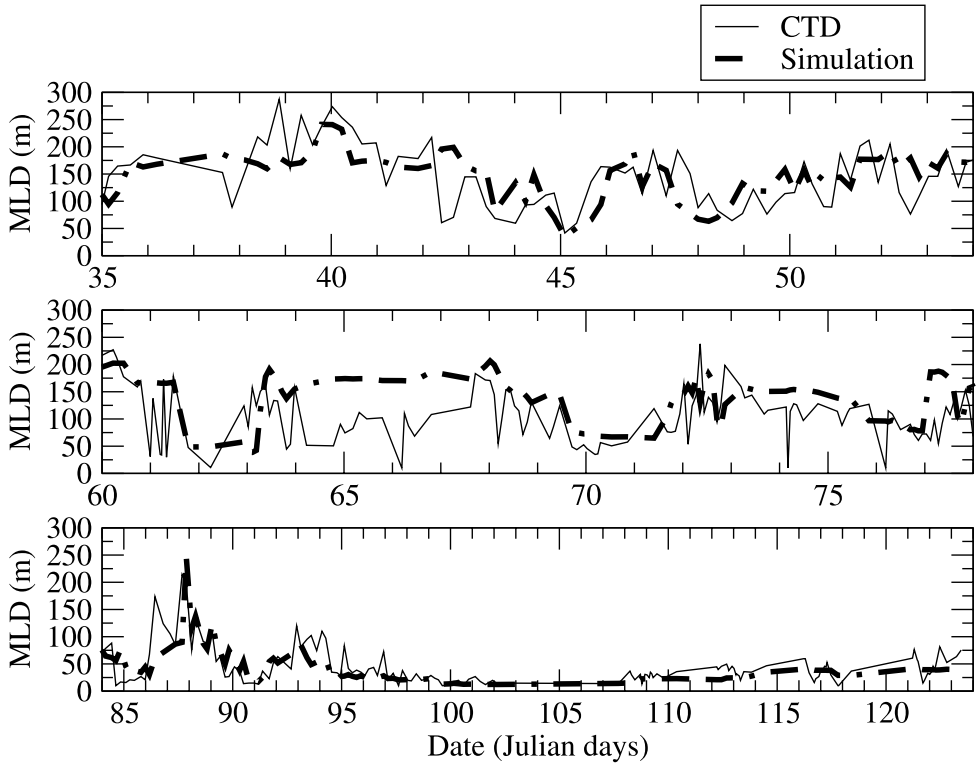

Figure 7. Comparison of the mixed layer depths deduced from CTD data collected along the ship track and from the simulation interpolated at the measurement points.

4.2.4. Vessel-Mounted Acoustic Doppler Current Profiler Currents

[48] Directly measured current data was collected by the vessel-mounted acoustic Doppler current profiler (VMADCP) (RDI, 75 kHz) between 3 February and 12 April. These currents are representative of the mean motion over the first 100 m below the surface and were filtered over a slipping 12 hours wide temporal window. VMADCP currents were sampled every 10 min and are compared with the simulated daily-averaged surface currents on Figure 8. The temporal filtering applied over the observed (12 hours) and the simulated (24 hours) data tends to remove the inertial waves and the ageostrophic component from the two signals. The correlation coefficients between the two time series is 0.74 for both the zonal and meridional components of the current during the P1 (11654 values) and P2 (13191 values) legs indicating that the simulated currents are in agreement with the observations. In fact, this agreement shows that the simulated geostrophic current, which results from the mass adjustment around the SOPRANE assimilated geostrophic guide, is close to the observed geostrophic current. This result confirms the good positioning of the main currents at a scale much better than one internal Rossby radius whereas the SOPRANE geostrophic current describes the circulation at best within three internal Rossby radius. Given the high spatial resolution and the great variability of the VMADCP data, this result is the most convincing validation because it points out the realism of structures smaller than *Ro* simulated by the model. Nevertheless, there are significant positive biases between the simulation and observations of the zonal component during the leg1 P2 (4 cm s^{-1}) and for the other time series (1.4 cm s^{-1} at maximum). These discrepancies can be attributed to errors in surface fluxes and SOPRANE geostrophic current analyses but also to the filtered VMADCP data which have an uncertainty of 1 cm s^{-1} (L. Prieur, personal communication, 2005).

5. Vertical Velocities and Mixed Layer Depths

[49] In order to see the respective influence of the mass and MLD fields on *w* during the spring 2001 period corresponding to intense heating and mixed layer shoaling, the daily-averaged vertical velocities on 22 March (onset of intense heating associated with moderate surface wind stress; $\tau \simeq 0.2$ N m^{-2}) at 200 m and 50 m depth were superimposed onto the surface dynamic height and the MLD fields respectively (Figures 9 and 10). Simulated *w* are not a representation of convection but result from the thermal wind imbalance between the simulated thermohaline field and the geostrophic guide (see system (1)).

[50] At 200 m depth, intense vertical velocities are found in areas of strong gradients of surface dynamic height (Figure 9) where the deformation field is strong. These regions correspond to the frontal zone on the southern flank of the cyclonic eddy C4 (42°N), the anticyclonic eddy A1 (43°N) and the stretched frontal line delimiting high and low dynamic height regions around 18°W, 40°N. Note that *w* velocities are structured in bands and are preferentially located on the periphery of the dynamic centers. This is particularly clear around A1 where positive *w* are found on its N-NW side and negative *w* on its S-SW side, whereas very weak *w* velocities are found in its center. Strong negative *w* on the southern flank of A1 illustrates the interaction between eddies A1 and C4.

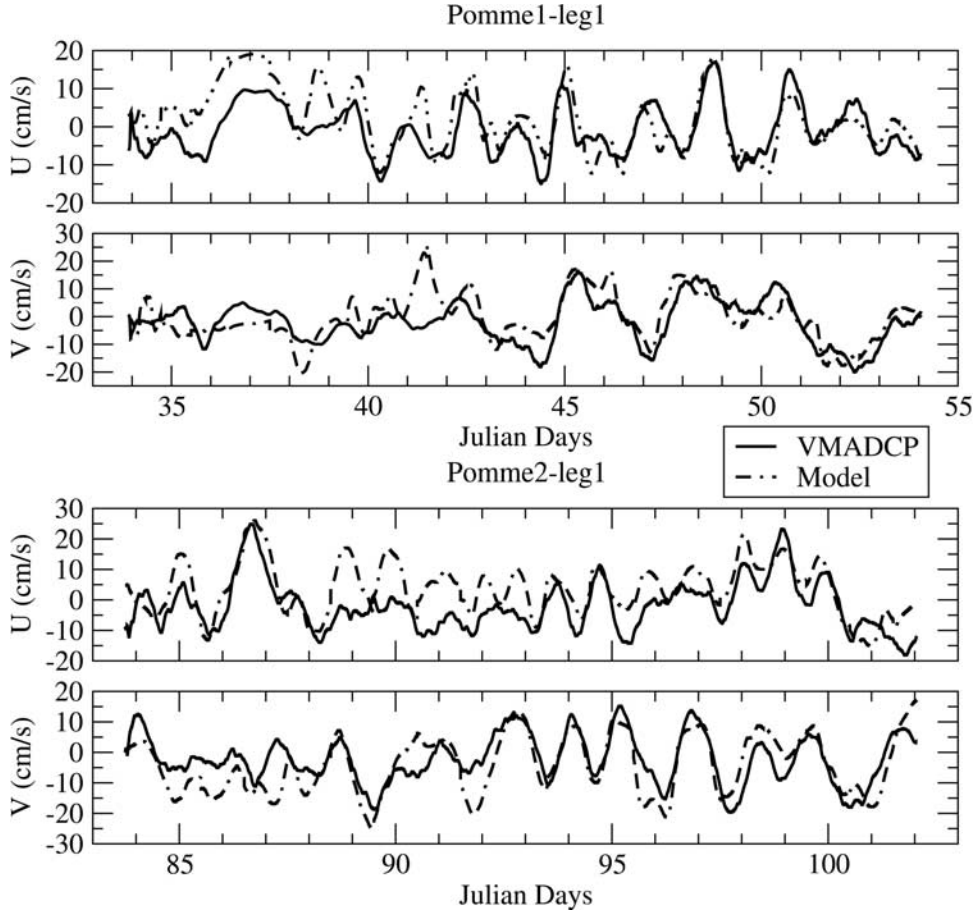

Figure 8. Comparison of vessel-mounted acoustic Doppler current profiler (VMADCP) measurements (averaged over the first 100 m below the surface) with simulated surface currents (cm s^{-1}) along the ship trajectory.

[51] Some *w* structures observed at 200 m are also found at 50 m, particularly those in association with the main dynamic centers. For example, the *w* structures peripherically distributed around A1 at 200 m are also found at 50 m (Figure 10). The MLD displayed on Figure 10 is in some places well correlated with the surface dynamic height (Figure 9), for example around A1, the meridional frontal line near 18°W, 40°N and in the vicinity of C4. Nevertheless, substantial differences exist between the *w* fields at 50 m and 200 m. Particularly, *w* at 50 m (Figure 10) displays a marked west-east filamentary and dipolar structure around 40.5° and 18.5°–20°W, which does not exist at 200 m. Moreover, this *w* structure adjusts well with the MLD gradient. Such *w* organization suggests that *w* could be related to the spatial distributions of heat and momentum fluxes at the surface and into the mixed layer whereas at 200 m the *w* structures could be induced by the mass deformation field. Causes which explain the *w* organizations at 200 m and 50 m are complex and need specific investigations. The important point is the emergence of energetic small horizontal scales near the surface found simultaneously in the *w* and MLD fields. Such submesoscale structures, not yet resolved by the observational data set, are also revealed by simulations of PE model [*Paci et al.*, 2005] and are of primary importance in order to perform realistic biological simulations [*Lévy et al.*, 2005]. In particular, concentrations of biological components are highly dependent on filamentary structures of MLD.

[52] In order to provide a quantitative estimate of the MLD and *w* structures present in the POMME domain, *Paci et al.* [2005] have performed an analysis of the horizontal scales simulated with a PE model. Their study has shown that shallowing occurs at the submesoscale and that the corresponding estimated length scale is of the order of 40 km; typically the scale of the filament identified in this section.

6. Mixed Layer Heat and Detrainment/Entrainment Budgets

6.1. Heat Budgets

[53] The heat budget in the mixed layer has been estimated during the annual run in a similar way as by *Caniaux and Planton* [1998]. The heat budget is expressed as

$$\begin{cases} \underbrace{\rho C_p h \dfrac{\partial \langle T \rangle}{\partial t}}_{\text{heat storage}} = \underbrace{-\rho C_p \left\{ h \langle \mathbf{U}_h \rangle \cdot \nabla \langle T \rangle + \nabla \cdot \displaystyle\int_{-h}^{0} \tilde{\mathbf{U}}_h \tilde{T} dz \right\}}_{\text{horizontal advection}} \\ \underbrace{-\rho C_p \{ \langle T \rangle - T(-h) \} \cdot w_e(-h)}_{\text{vertical transport}} + \underbrace{F_{\text{sol}} \{ I(0) - I(-h) \} + F_{n\text{sol}}}_{\text{net surface heat flux}}, \\ + \underbrace{\rho C_p \overline{w'T'}(-h)}_{\text{turbulent entrainment}} \end{cases} \quad (2)$$

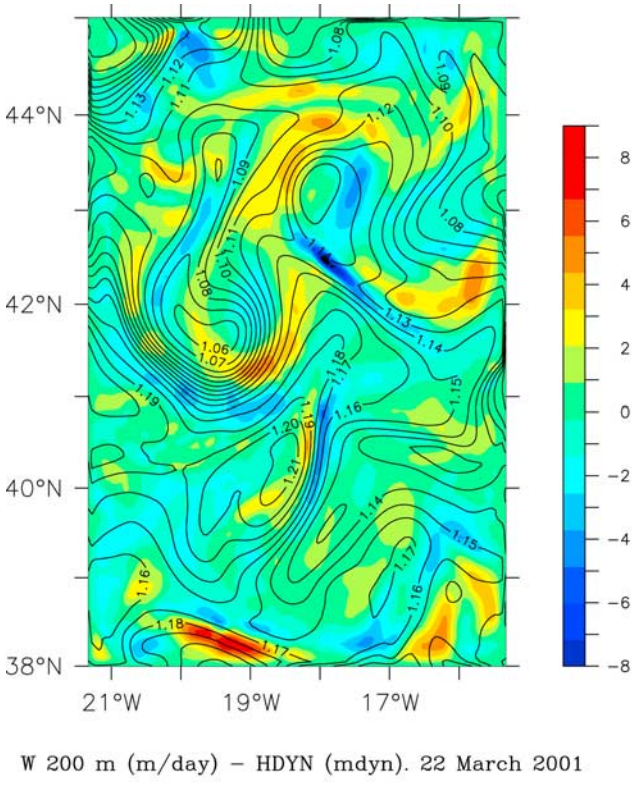

Figure 9. Daily averaged vertical velocity at 200 m superimposed onto the surface dynamic height on 22 March. The surface dynamic height is computed from the 1000 m reference level.

where

$$\langle X \rangle = \frac{1}{h} \int_{-h}^{0} X dz$$

$$\tilde{X} = X - \langle X \rangle,$$

and where $h = h(x, y, t)$ is the depth of the mixed layer ($\Delta\rho = \rho(z = 12.5\ \text{m}) + 0.02\ \text{kg m}^{-3}$) at the point x, y and time t; X stands for temperature T and the horizontal current $\mathbf{U}_h$; F_{sol} is the shortwave radiation; $I(z)$ its transmission at depth z; $F_{n\text{sol}}$ is the nonsolar surface heat flux, the sum of the sensible, latent, and net infrared heat fluxes; $\overline{w'T'}$ is the classic notation for turbulent heat flux. The vertical flow of mass or entrainment rate across the evolving surface $z = -h$ is

$$w_e(-h) = w_h + \partial_t h + \mathbf{U}_h \cdot \nabla h.$$

The left-hand side of equation (2) represents the heat storage or heat budget noted H. The terms on the right-hand side are the horizontal heat advection by the depth-averaged current and by its deviation from this mean current; the vertical transport corresponding to the flux of heat carried by the particles of fluid across the surface $z = -h$; the net surface heat flux including the extinction of the surface solar flux with depth; and the turbulent entrainment corresponding to the turbulent heat flux across the surface $z = -h$.

6.1.1. Results: Averaged One-Dimensional

[54] Figure 11 is a time plot of the time cumulative domain averaged budget in W m^{-2} obtained by dividing each term of the mixed layer heat budget by the total cumulative time (343 days). A zero value has been chosen as the initial value. Given the evolution of the heat budget, two periods can be distinguished: before 17 March the period of mixed layer cooling and after this date the period of mixed layer heating. This evolution is the same as the net surface heat flux that stresses the necessity to have accurate radiative and turbulent surface fluxes to force the model. The mixed layer energetic loss reaches the maximum of -44 W/m^2 on 17 March when the contribution of the net surface heat flux rises up to -36 W/m^2. The vertical transport and the turbulent entrainment have linear trends whereas the horizontal advection increases rapidly up to 17 March and stabilizes afterward. As a result, during winter, the horizontal advection plays an important role in the mixed layer cooling. On 17 March, the horizontal advection contributes to -7.4 W m^{-2} of the budget and the entrainment and vertical transport are weak and of opposite sign of the order of 1 W m^{-2}. After 17 March, the mixed layer heating and restratification occur as a result of the net surface heat flux increase. This increase is weakly modulated by the contributions of the others components. Indeed, the horizontal advection trend is still negative but is

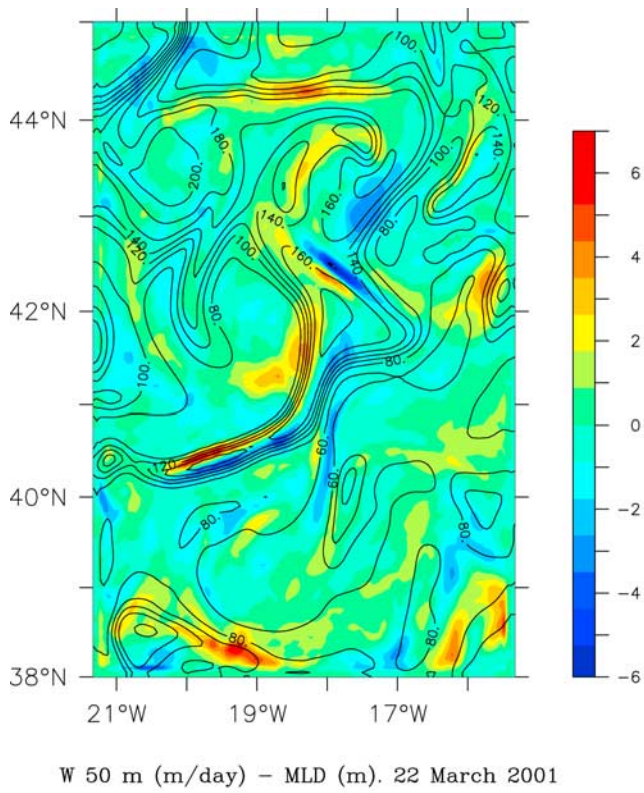

Figure 10. Daily averaged vertical velocity at 50 m superimposed onto the mixed layer depth on 22 March. Onset of intense heating associated with moderate surface stress; $\tau \simeq 0.2$ N m^{-2}.

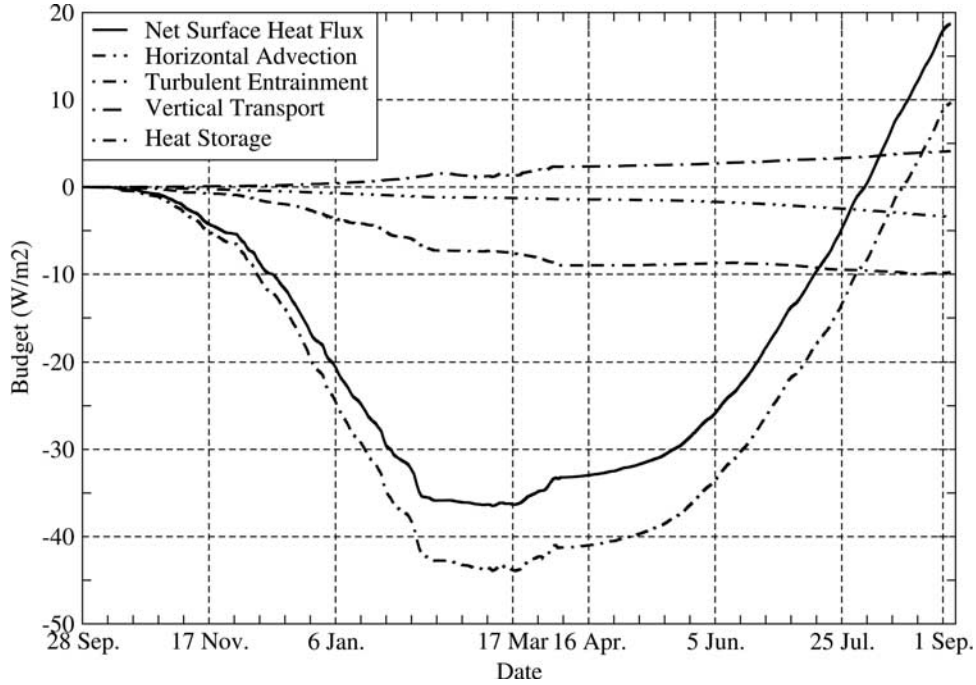

Figure 11. Annual evolution of the cumulative domain-averaged mixed layer heat budget. Units are in W m^{-2}, obtained by dividing each term of the mixed layer heat budget by the total cumulative time (343 days).

particularly weak during the heating period due to weaker mesoscale activity and weaker Ekman currents in comparison with the cooling period. Note also the more pronounced increase of the vertical transport after 17 March due to the MLD shallowing during this period. Such behavior can also be found by *McCulloch and Leach* [1998]. On 4 September, H reaches 9.7 W m^{-2}. This value is positive, which is consistent with SSTs greater at P3 than at P0. The heat budget H is supplied by the net surface heat flux (18.7 W m^{-2}) and the vertical transport (4.1 W m^{-2}) and is compensated by the turbulent entrainment (-3.4 W m^{-2}) and the horizontal advection (-9.7 W m^{-2}). Using a model based on a simplified Kalman filter, *Gaillard et al.* [2005] confirm the values of heat storage and horizontal advection found in this study.

[55] It is interesting now to put into perspective some components of this regional mixed layer heat budget with respect to the components of climatological upper layers heat budgets in the POMME region.

[56] Using the heat flux climatologies provided by *Isemer and Hasse* [1987], *Marshall et al.* [1993] broadly obtained a surface buoyancy input of -10 W m^{-2} over the POMME domain that represents a negative bias of nearly -20 W m^{-2} compared to our estimate. This substantial uncertainty could be partly due to interannual variability that is confirmed by *Weller et al.* [2004] and *Caniaux et al.* [2005b].

[57] The annual domain-averaged vertical heat transport calculated in this study (4.1 W m^{-2}) (Figure 11) is close to the climatological Ekman pumping estimate (6 W m^{-2}) given by *Marshall et al.* [1993] and *McCulloch and Leach* [1998].

[58] The climatological seasonal heat budget of the upper 500 m calculated by *McCulloch and Leach* [1998] over the North Atlantic roughly splits the domain POMME into -10 W m^{-2} for the geostrophic and -14 W m^{-2} for the Ekman drift advection. In this study, the annual total horizontal advection was evaluated close to -10 W m^{-2} and confirmed by *Caniaux et al.* [2005b] which splits this value into -14 W m^{-2} for the Ekman drift and 4 W m^{-2} for the geostrophic advection. Although the heat budget was carried out here over the evolving MLD, a good agreement with *McCulloch and Leach* [1998] is obtained for the Ekman drift component while the geostrophic component has the opposite sign compared with the climatological estimate. This can be explained by the significant interannual variability of the geostrophic currents in the POMME region [*Reverdin et al.*, 2005].

[59] Finally, note that *McCulloch and Leach* [1998] indicate a stronger contribution of the Ekman drift flux compared with the Ekman pumping flux for the upper-layer heat budget while *Marshall et al.* [1993] suggest the opposite. This illustrates the uncertainties which affect the components of the heat budget in the POMME domain.

6.1.2. Results: Two-Dimensional

[60] The two-dimensional plots displayed in Figure 12 show the spatial variability of H and each of its terms. H and its components have been integrated over the depth of the mixed layer and time integrated during the run and then time averaged. The turbulent entrainment at the mixed layer base is not shown because it is spatially quite uniform and of the order of -3 W m^{-2}.

[61] Mesoscale structures of H are mainly explained by the horizontal advection, especially in the frontal region (-40 W m^{-2}) between 41°N and 42°N, around the anticyclonic eddy A1 and along a corridor in the southwestern part of the domain associated with a marked southwestward current. The advection component is highly driven by the mesoscale circulation which impacts H more effectively

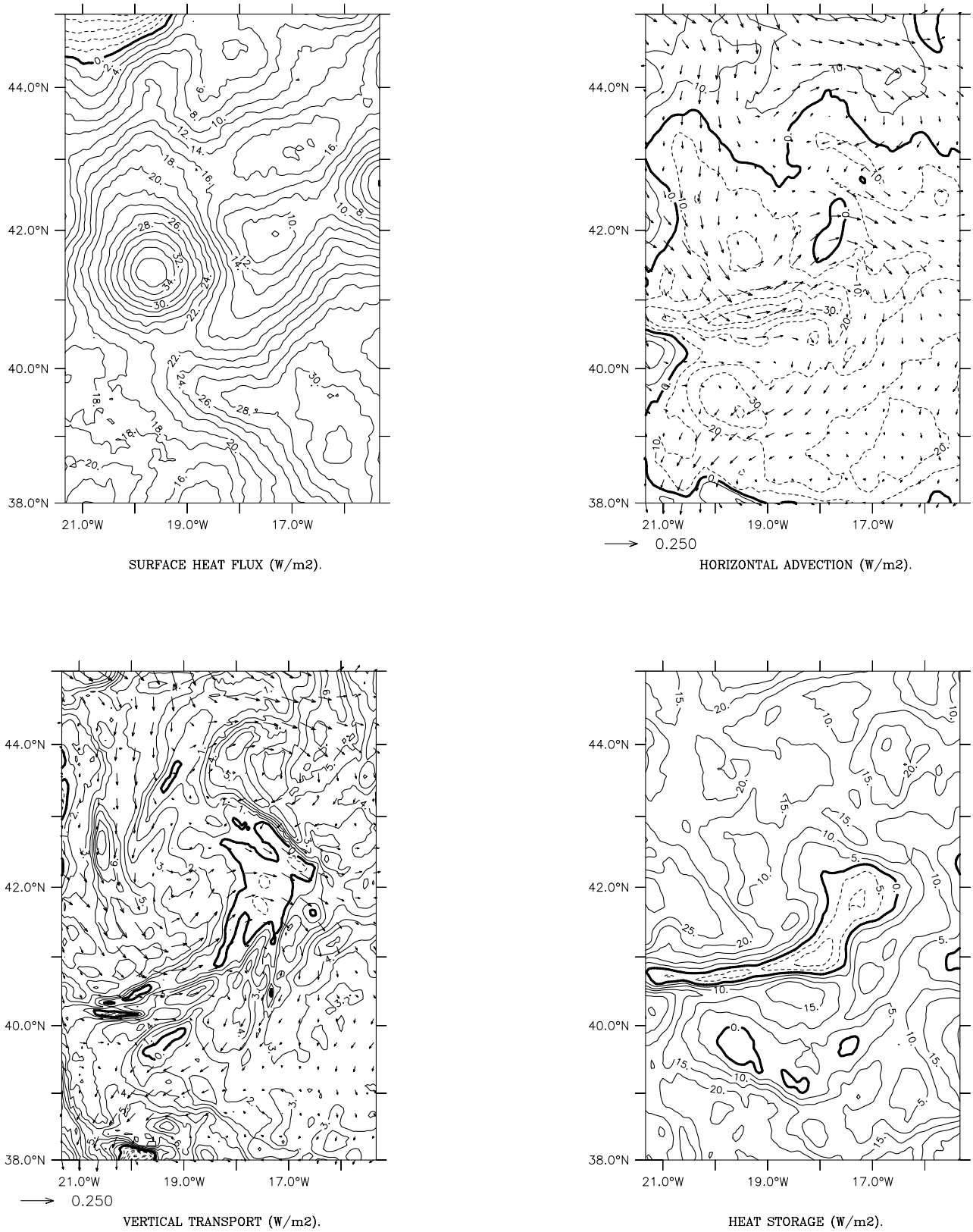

Figure 12. Annual mean charts of each term of the mixed layer heat budget. Units are in W m^{-2}, obtained by dividing each term of the mixed layer heat budget by the total cumulative time (343 days). The annual mean surface current (m s^{-1}) is superimposed onto the horizontal advection and vertical heat transport. Contour intervals are 2 W m^{-2} for surface heat flux; 10 W m^{-2} for horizontal advection; 1 W m^{-2} for vertical transport; and 5 W m^{-2} for the mixed layer heat budget.

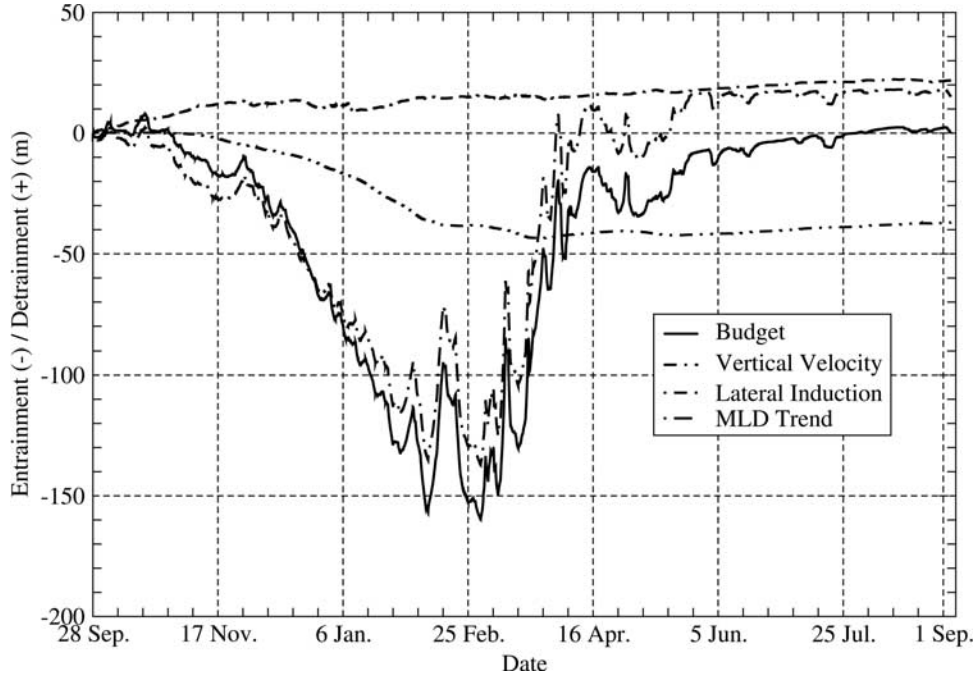

Figure 13. Annual evolution of the cumulative domain-averaged mixed layer detrainment-entrainment (m).

than the net surface heat flux. Some modulations of H result from the vertical transport where the signal is well correlated to the mesoscale structures of the year-averaged circulation. In particular, the main negative region between 40°N and 43°N corresponds to the ascending branch surrounding C4 and reaching to A1. These mean structures are not spurious effects of the averaging procedure but really correspond to the quasi-permanent positions of C4 and A1 during POMME as mentioned in section 2.3. Note the strong gradients near 43°N corresponding to the interaction zone between C4 and A1. Stronger positive values (6 W m^{-2}) are found around the periphery of the anticyclonic eddy A1 where maxima of w were also found. Stronger positive values (8 W m^{-2}) are also found along the western side of the cyclonic eddy C4 where an intense southward circulation occurs. The vertical transport structures are submesoscale in size because (1) the vertical velocity restores the geostrophic balance in the fluid over smaller scales than the horizontal ageostrophic circulation and (2) the MLD has strong temporal and spatial variability.

[62] In contrast to the time cumulative domain average, the spatial repartition of H does not have the same signature as the net surface heat flux because of a strong heat redistribution in the POMME domain mainly by horizontal advection at the mesoscale and submesoscale.

6.2. Detrainment-Entrainment Budget

[63] An estimate of the annual mass flux through the evolving mixed layer depth $z = -h(x, y, t)$ is proposed in this section in order to go further in the analysis of the simulation. The instant detrainment (+) or entrainment (−) rate in three-dimensional mixed layer models is defined as [*de Szoeke*, 1980; *Cushman-Roisin*, 1987]

$$D = -(w_h + \mathbf{U}_h \cdot \nabla h + \partial_t h), \tag{3}$$

where w_h and $\mathbf{U}_h$ are the vertical and horizontal velocities at the base of the mixed layer, and h is the depth of the mixed layer. The annual detrainment-entrainment budget corresponding to the net mass flux S through the surface $z = -h(x, y, t)$ is

$$S = \int_0^T D \cdot dt, \tag{4}$$

where $t = 0$ is the initial time P0 and $t = T = 345$ days the final time P3. Water released from the mixed layer (detrainment) is counted positively when water included in the mixed layer (entrainment) is counted negatively. The components of the budget S are

Vertical velocity

$$-\int_0^T w_h \cdot dt,$$

Lateral induction

$$-\int_0^T \mathbf{U}_h \cdot \nabla h \cdot dt,$$

Mixed layer depth trend

$$-\int_0^T \partial_t h \cdot dt.$$

6.2.1. Results: Averaged One-Dimensional

[64] The time-cumulative domain averaged budget in meters is presented Figure 13. The evolution of the budget describes a closed annual cycle: the water entrained into the mixed layer during autumn and winter is completely detrained during spring and summer. Note also that the

entrainment and detrainment periods are strongly asymmetric since they last 5 months (October–February) and 1.5 months (March–16 April) respectively. This asymmetry is explained by the annual MLD trend (see section 4.2.1). This component contributes to the significant entrainment of water into the mixed layer induced by a slow MLD deepening which occurs up to 25 February. During March and the first half part of April, the detrainment is induced by a rapid shallowing. At the end of the simulation, the cumulated MLD trend contributes to detrainment (15.1 m). This positive value corresponds to a shallower mixed layer at P3 (4 September) than at P0 (28 September). The vertical velocity component is a positive contribution to S, which reaches 22 m of detrained water at the end of the simulation. Its evolution is positive because the averaged w_h over the domain is generally always negative (downwelling). This large-scale downwelling motion is induced by the permanent anticyclonic surface wind over the subtropical gyre. Note that the positive tendency of w_h is stronger after 17 March, due to the reinforced anticyclonic gyre signal compared to weakened mesoscale activity in spring and summer. The lateral induction actively contributes to entrain water in the mixed layer during autumn and winter. The maximum of entrained water reaches −43.4 m on 17 March. After this date, the trend becomes weakly positive, corresponding to detrainment. At the end of the simulation, the contribution of lateral induction is of −37 m. Thus the detrained water during spring and summer by lateral induction reaches 6.4 m.

[65] To our knowledge, there are no estimations of yearlong mixed layer detrainment/entrainment budget in the POMME region, consequently we propose to compare our results to climatological estimations of subduction derived from the kinematic method, when it is possible. This method splits subduction into vertical velocity and lateral induction components [*Marshall et al.*, 1993]. For the vertical velocity, a large consensus is achieved of around 20–25 m yr^{-1} [*Marshall et al.*, 1993; *McLaren and Williams*, 2001; *Spall et al.*, 2000]. Although these results refer only to subduction and not detrainment, our result (22 m yr^{-1}) is in the same bulk range because the vertical velocities of the deepest winter mixed layer and the evolving mixed layer do not differ significantly.

6.2.2. Results: Two-Dimensional

[66] The two-dimensional plots of the detrainment/entrainment budget in Figure 14 show the spatial variability of each term of S. S and its components have been time integrated during the run and then time averaged. Positive values correspond to detrainment while negative values correspond to entrainment.

[67] Although the cumulative-averaged budget S does not indicate large detrainment or entrainment at the scale of the domain, the two-dimensional S field shows three key detrainment areas. The first area is around the anticyclonic eddy A1, the second on the western side of the cyclonic eddy C4 and the third along a band or corridor located in the southeast of the domain and directed NE (42°N, 17°W) SW (39°N, 19°W) in association with a marked southwestward current.

[68] Averaged over the domain, S is mainly driven by the MLD trend but when plotted, S is explained by lateral induction that represents the horizontal water transport by the current $\mathbf{U}_h$ through the evolving surface $z = -h(x, y, t)$. This component clearly explains most of the mesoscale and submesoscale structures of the S field, particularly in the three key detrainment areas. This result is due to the combined effects of the mesoscale circulation (see Figure 14), which is strongly structured by A1, C4 and A2 (see section 2.3), and strong MLD gradients taking also place around these structures. The three key detrainment areas include mesoscale and submesoscale structures of 100 m and 300 m intensity respectively. Strong negative values (−160 m) of entrained water are also found in the frontal zone around 41°N where strong currents and strong MLD gradients exist. Observational data sets have identified eddy trains tracking from the northeast to southwest [*Le Cann et al.*, 2005]. Given that numerous observed tracks of eddies are included in the above-cited NE-SW corridor, this active detrainment area could be associated with these eddies trains as already mentioned by *Rudnick and Luyten* [1996].

[69] Although the values of lateral induction found in this study cannot be compared to subduction values, Figure 14 highlights the large mesoscale contribution of lateral induction in detrainment which could be important for subduction as mentioned by *Valdivieso da Costa et al.* [2005].

[70] The vertical velocity component has two characteristics: (1) the signal is mainly positive and globally contributes to detrainment from 20 to 40 m, except in the frontal zone near 40.5°N and the interaction zone between the cyclonic (C4) and anticyclonic (A1) eddies (42°N); (2) the w signal also includes submesoscale structures that reinforce and make more complex the lateral induction mesoscale structures. Thus the w signal splits up into (1) a downwelling large-scale component induced by the surface wind forcing over the subtropical gyre and (2) a submesoscale component.

[71] Finally, the MLD trend component, which explains the cumulative domain-averaged budget evolution, is quite homogenous over the domain (10–20 m): this is a large-scale component. Positive values of detrainment result everywhere at shallower MLDs at P3 compared with P0.

7. Summary

[72] This paper presents a 1 year mesoscale simulation in the northeast Atlantic during the POMME experiment (September 2000–2001). This model is based on a simplified primitive equation system obtained by the assimilation of analysis-derived geostrophic currents into the momentum equation as a substitution of the horizontal pressure gradient. In this system, the time sequence of geostrophic currents is provided by weekly optimal analyses from a quasi-geostrophic model assimilating altimetry data during POMME. This original assimilation technique avoided strong model drift during 1 year as well as shocks usually induced by sequential assimilation methods and the computation of propagating radiative velocity at the lateral boundaries.

[73] The main objective of this paper was to show that the simplified model was able to simulate the observed mesoscale and submesoscale thermohaline, circulation and mixed layer structures associated with cyclonic/anticyclonic eddies and fronts during the 1 year POMME Experiment. This objective was achieved due to the use of (1) a guided

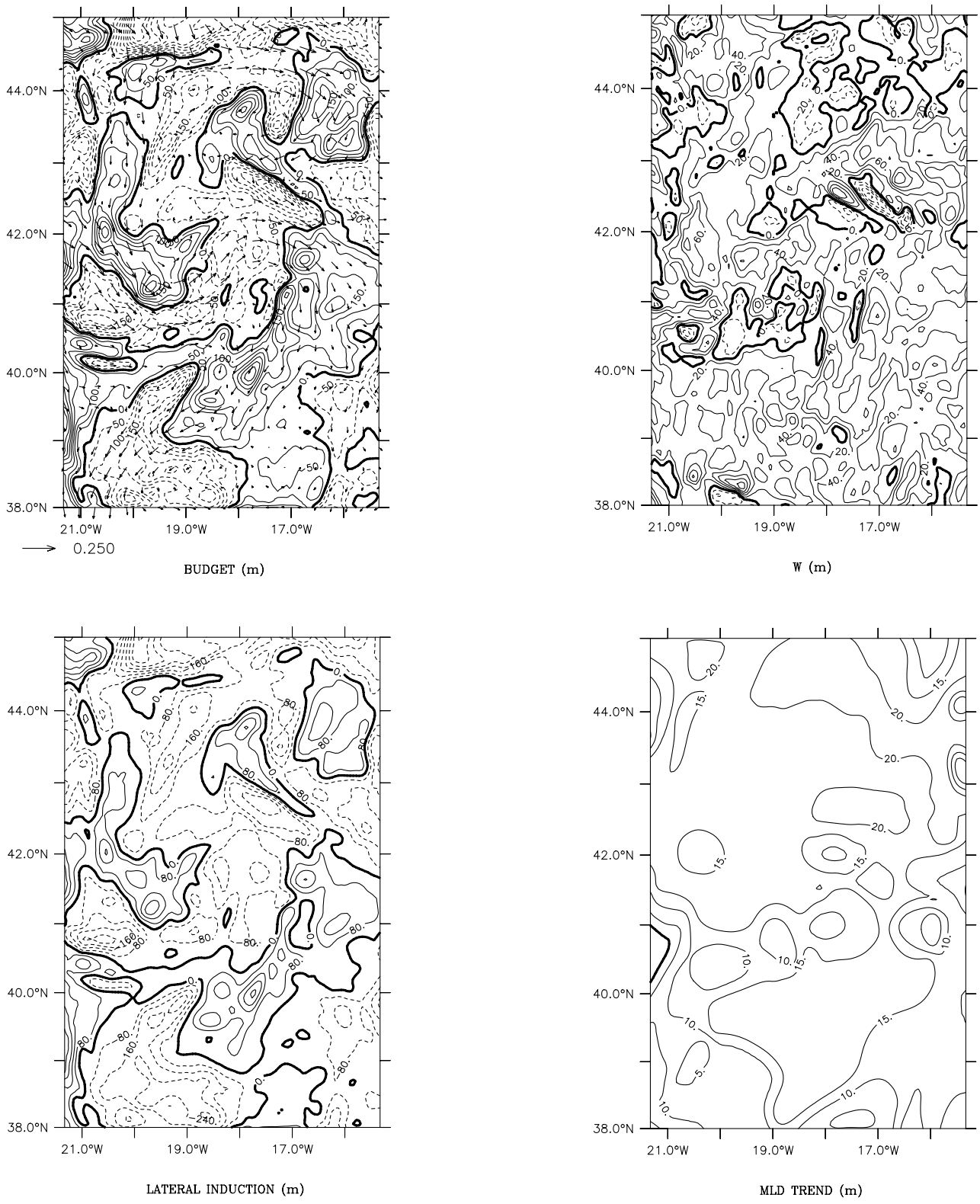

Figure 14. Annual mean charts of each term of the mixed layer detrainment-entrainment (m). The annual mean surface current (m s^{-1}) is superimposed onto the detrainment-entrainment budget (S). Contour intervals are 50 m for the budget; 20 m for W; 80 m for lateral induction; and 5 m for the mixed layer depth trend.

geostrophic adjustment, (2) realistic surface fluxes, and (3) adequate lateral boundary conditions. Intense w structures were found preferentially at the periphery of the eddies where the deformation field is presumed to be strong. Another important point was the emergence of energetic small horizontal scales near the surface in the w and mixed layer depth fields. On the basis of the accurate validation carried out against the POMME/satellite analyses, CTD, thermosalinograph and VMADCP data, we conclude that this simplified model is particularly well adapted to perform yearlong mixed layer budgets.

[74] During POMME, the mixed layer stored 9.7 W m^{-2}. This budget was supplied by the net surface heat flux (18.7 W m^{-2}) and the vertical transport (4.1 W m^{-2}) and was compensated by the turbulent entrainment (-3.4 W m^{-2}) and the horizontal advection (-9.7 W m^{-2}). From these results, the mixed layer heat budget in the POMME domain can be roughly deduced from the net surface heat flux and horizontal advection balance.

[75] The simulated yearlong cumulative domain-averaged detrainment-entrainment budget is null and its components are distributed as follows: MLD trend (detrainment: 15 m), vertical velocity (detrainment: 22 m), and lateral induction (entrainment: -37 m).

[76] The two-dimensional representation of the mixed layer heat and mass budgets clearly reveals the mesoscale and submesoscale patterns of these fields. These structures are unambiguously explained by the temperature horizontal advection for the mixed layer heat storage and by the lateral induction for the detrainment/entrainment budget, which are associated with the mesoscale eddies A1, C4 and A2 and the front around 41°N. The two-dimensional mass budget shows three key detrainment areas that are (1) around the annual averaged anticyclonic eddy A1, (2) on the western side of the annual averaged cyclonic eddy C4, and (3) in a corridor directed northeast southwest in the southeast of the domain. These areas were also found to be the seat of intense negative thermal advection. These mesoscale zones were associated with the dynamically active centers A1, C4, A2 and the front, not only because strong horizontal currents and MLD gradients were simultaneously found but mainly because these centers were quasi-permanent during POMME. This point is particularly important because these dynamic centers have structured the mesoscale circulation during POMME. The direct consequence of this result is the identification of privileged mesoscale and submesoscale advective structures. This means that the annual averaged circulation is representative of the mesoscale flow during POMME.

[77] Mixed layer heat and detrainment/entrainment mesoscale structures were mainly explained by the thermal advection and the lateral induction but were enriched on finer scales (submesoscale) by the vertical velocity. Although the downward w signal has a subtropical anticyclonic gyre-scale component induced by the surface wind stress it also has a submesoscale component associated with the internal geostrophic adjustment of the dynamic centers mentioned above and, probably, with the small-scale variability of the surface fluxes. Although no dynamical observational data set makes it possible to validate these detrainment regions, it is interesting to mention that these regions are confirmed by primitive equation simulations (A. Paci et al., manuscript in preparation, 2005) and correspond to maxima of oxygen concentrations observed during POMME (L. Prieur, personal communication, 2005): these are consistent independent results.

[78] **Acknowledgments.** The authors acknowledge the SHOM/CMO for giving its authorization to use and publish the QG model results from SOPRANE system in a scientific framework. We are grateful to Anna Pirani for her help in revising this manuscript, to the scientific staff of the POMME programm, L. Mémery and G. Reverdin, to the ship principal scientists, Y. Desaubies and J. Paillet (POMME 0), L. Prieur and F. Herpes (POMME 1), M. Bianchi and J. Paillet (POMME 2), and J. C. Gascard (POMME 3). We wish to thank the three anonymous reviewers for their comments, which helped to improve and clarify this paper. This work was supported by the French programs PATOM and PROOF (CNRS/INSU).

References

Assenbaum, M., and G. Reverdin (2005), Near real-time analyses of the mesoscale circulation during the POMME experiment, *Deep Sea Res., Part I*, in press.

Barnier, B., L. Siefridt, and P. Marchesiello (1995), Thermal forcing for a global ocean circulation model using a three year climatology of ECMWF analyses, *J. Mar. Syst.*, *6*, 363–380.

Blayo, E., J. Verron, and J. M. Molines (1994), Assimilation of TOPEX/Poseidon altimeter data into a circulation model of the North Atlantic, *J. Geophys. Res.*, *99*, 24,691–24,705.

Bougeault, P., and P. Lacarrère (1989), Parameterization of orography-induced turbulence in a meso-beta scale model, *Mon. Weather Rev.*, *117*, 1872–1890.

Brisson, A., P. Leborgne, A. Marsouin, and T. Moreau (1994), Surface irradiances calculated from Meteosat sensor data during SOFIA-ASTEX, *Int. J. Remote Sens.*, *15*, 197–203.

Caniaux, G., and S. Planton (1998), A three-dimensional ocean mesoscale simulation using data from the SEMAPHORE experiment: Mixed layer heat budget, *J. Geophys. Res.*, *103*, 25,081–25,099.

Caniaux, G., A. Brut, D. Bourras, H. Giordani, A. Paci, L. Prieur, and G. Reverdin (2005a), A 1 year sea surface heat budget in the northeastern Atlantic basin during the POMME experiment: 1. Flux estimates, *J. Geophys. Res.*, *110*, C07S02, doi:10.1029/2004JC002596.

Caniaux, G., S. Belamari, H. Giordani, A. Paci, L. Prieur, and G. Reverdin (2005b), A 1 year sea surface heat budget in the northeastern Atlantic basin during the POMME experiment: 2. Flux optimization, *J. Geophys. Res.*, *110*, C07S03, doi:10.1029/2004JC002695.

Carpenter, K. (1982), Radiation conditions for lateral boundaries of limited area numerical models, *Q. J. R. Meteorol. Soc.*, *110*, 717–719.

Cushman-Roisin, B. (1987), *Dynamics of the Oceanic Surface Mixed-Layer*, edited by P. Muller, and D. Henderson, special publication, Hawaii Inst. of Geosphys., Honolulu.

de Mey, P., and M. Benkiran (2000), A multivariate reduced-order optima interpolation method and its application to the Mediterranean basin-scale circulation, in *Ocean Forecasting: Conceptual Basis and Application*, edited by N. Pinardi, pp. 281–306, Springer, New York.

de Mey, P., and P. Ménard (1989), Synoptic analysis and dynamical adjustment of GEOS-3 and SEASAT altimeter eddy fields in the northwest Atlantic, *J. Geophys. Res.*, *94*, 6221–6230.

de Szoeke, R. (1980), On the effects of horizontal variability of wind stress on the dynamics of the ocean mixed layer, *J. Phys. Oceanogr.*, *10*, 1439–1454.

Dourado, M., and G. Caniaux (2001), Surface heat budget in an oceanic simulation using data from Tropical Ocean–Global Atmosphere Coupled Ocean-Atmosphere Response Experiment, *J. Geophys. Res.*, *106*, 16,623–16,640.

Drijfhout, S., and F. Walsteijn (1998), Eddy-induced heat transport in a coupled ocean-atmospheric anomaly model, *J. Phys. Oceanogr.*, *28*, 250–265.

Fernández, C. I., P. Raimbault, N. Garcia, P. Rimmelin, and G. Caniaux (2005), An estimation of annual new production and carbon fluxes in the northeast Atlantic Ocean during 2001, *J. Geophys. Res.*, *110*, C07S13, doi:10.1029/2004JC002616.

Gaillard, F., H. Mercier, and C. Kermabon (2005), A synthesis of the POMME physical data set: One year monitoring of the upper layer, *J. Geophys. Res.*, *110*, C07S07, doi:10.1029/2004JC002764.

Gavart, M. (1996), Modélisation et assimilation de données dans un modèle de circulation océanique à méso-échelle: Application à la campagne SEMAPHORE, Ph.D. thesis, Univ. Paul Sabatier, Toulouse, France.

Gavart, M., and P. de Mey (1997), Isopycnal EOFs in the Azores current region: A statistical tool for dynamical analysis ans assimilation, *J. Phys. Oceanogr.*, *27*, 2146–2157.

Giordani, H., G. Caniaux, and L. Prieur (2005), A simplified oceanic model assimilating geostrophic currents: Application to the POMME experiment, *J. Phys. Oceanogr.*, *35*, 628–644.

Isemer, H., and L. Hasse (1987), *The Bunker Climate Atlas of the North Atlantic Ocean*, vol. 2, 252 pp., Springer, New York.

Le Cann, B., M. Assenbaum, J.-C. Gascard, and G. Reverdin (2005), Observed mean and mesoscale upper ocean circulation in the midlatitude northeast Atlantic, *J. Geophys. Res.*, *110*, C07S05, doi:10.1029/2004JC002768.

Lermusiaux, P., and A. Robinson (1999), Data assimilation via error subspace statistical estimation. Part I: Theory and schemes, *Mon. Weather Rev.*, *127*, 1385–1407.

Leslie, L. M., G. A. Miles, and D. J. Gauntlett (1981), The impact of FGGE data coverage and improved numerical techniques in numercial weather prediction in the Australian region, *Q. J. R. Meteorol. Soc.*, *107*, 627–642.

Levitus, S. (1982), Climatological atlas of the world ocean, *NOAA Prof. Pap.*, *13*, 173 pp.

Lévy, M., M. Gavart, L. Mmery, G. Caniaux, and A. Paci (2005), A four-dimensional mesoscale map of the spring bloom in the northeast Atlantic (POMME experiment): Results of a prognostic model, *J. Geophys. Res.*, *110*, C07S21, doi:10.1029/2004JC002588.

Lozano, C., A. Robinson, H. Arango, A. Gangopadhyay, N. Sloan, P. Haley, and W. Leslie (1996), *An Interdisciplinary Ocean Prediction System: Assimilation in Strategies and Structured Data Models: Modern Approaches to Data Assimilation in Ocean Modelling*, *Oceanogr. Ser.*, vol. 61, edited by P. Malanotte-Rizzoli, pp. 413–452, Elsevier, New York.

Marshall, J., A. Nurser, and R. Williams (1993), Inferring the subduction rate and period over the North Atlantic, *J. Phys. Oceanogr.*, *23*, 1315–1329.

McCulloch, M., and H. Leach (1998), Air-sea fluxes inferred from an upper ocean heat budget north-east of the Azores, *Q. J. R. Meteorol. Soc.*, *124*, 2465–2476.

McLaren, A., and R. Williams (2001), Interannual variability in the thermodynamics of subduction over the North Atlantic, *J. Phys. Oceanogr.*, *31*, 3284–3294.

Mémery, L., G. Reverdin, J. Paillet, and A. Oschlies (2005), Introduction to the POMME special section: Thermocline ventilation and biogeochemical tracer distribution in the northeast Atlantic Ocean and impact of mesoscale dynamics, *J. Geophys. Res.*, doi:10.1029/2005JC002976, in press.

Paci, A., G. Caniaux, M. Gavart, H. Giordani, M. Lévy, L. Prieur, and G. Reverdin (2005), A high-resolution simulation of the ocean during the POMME experiment: Simulation results and comparison with observations, *J. Geophys. Res.*, doi:10.1029/2004JC002712, in press.

Paillet, J., and M. Arhan (1996), Shallow pycnoclines and mode water subduction in the eastern North Atlantic, *J. Phys. Oceanogr.*, *26*, 96–114.

Reverdin, G., M. Assenbaum, and L. Prieur (2005), Eastern North Atlantic Mode Waters during POMME (September 2000 – 2001), *J. Geophys. Res.*, *110*, C07S04, doi:10.1029/2004JC002613.

Robinson, A. (1996), Physical processes, field estimation and interdisciplinary ocean modelling, *Earth Sci. Rev.*, *40*, 3–54.

Robinson, A., P. Lermusiaux, and N. Q. Sloan (1998), Data assimilation, in *The Sea: The Global Coastal Ocean*, vol. 1, *Processes and Methods*, pp. 541–594, John Wiley, Hoboken, N. J.

Rudnick, D. L., and J. R. Luyten (1996), Intensive surveys of the Azores Front: 1. Tracers and dynamics, *J. Geophys. Res.*, *101*, 923–939.

Spall, M., R. Weller, and P. Furey (2000), Modeling the three-dimensional upper ocean heat budget and subduction rate during the Subduction Experiment, *J. Geophys. Res.*, *103*, 15,817–15,831.

Stramma, L. (1984), Geostrophic transport in the warm water sphere of the eastern subtropical North Atlantic, *J. Mar. Res.*, *42*, 537–558.

Valdivieso da Costa, M., H. Mercier, and A. Tréguier (2005), Effects of the mixed-layer time variability on kinematic subduction rate diagnostics, *J. Phys. Oceanogr.*, *35*, 427–443.

Weller, R., P. Furey, M. Spall, and R. Davis (2004), The large-scale context for oceanic subduction in the northeast Atlantic, *Deep Sea Res., Part I*, *51*, 665–699.

Xue, M., and A. Thorpe (1991), A mesoscale numerical model using non-hydrostatic pressure-based sigma coordinate equations: Model experiments with dry mountain flows, *Q. J. R. Meteorol. Soc.*, *119*, 1168–1185.

G. Caniaux, H. Giordani, and A. Paci, Meteo-France/Centre National de Recherches Météorologiques/Groupe d'Etudes de l'Atmosphère Météorologique, 42 av. G. Coriolis, F-31057 Toulouse Cedex 01, France. (herve.giordani@meteo.fr)

S. Giraud, Service Hydrologique et Océanographique de la Marine/Centre Militaire d'Océanographie/Recherche, Observatoire Midi-Pyrénées, 14 avenue E. Belin, F-31400 Toulouse, France.

L. Prieur, Laboratoire d'Océanographie de Villefranche, BP 28, F-06234 Villefranche-sur-mer Cedex, France.